

## Observation of photon-nucleus angular-momentum transfer in the strong-field breaking of molecules

Xiaochun Gong,<sup>1,\*</sup> Peilun He,<sup>2,\*</sup> Junyang Ma,<sup>1</sup> Wenbin Zhang,<sup>1</sup> Fenghao Sun,<sup>1</sup> Qinying Ji,<sup>1</sup> Kang Lin,<sup>1</sup> Hanxiao Li,<sup>1</sup> Junjie Qiang,<sup>1</sup> Peifen Lu,<sup>1</sup> Hui Li,<sup>1</sup> Heping Zeng,<sup>1</sup> Jian Wu,<sup>1,3,†</sup> and Feng He<sup>2,‡</sup>

<sup>1</sup>State Key Laboratory of Precision Spectroscopy, East China Normal University, Shanghai 200062, China

<sup>2</sup>Key Laboratory of Laser Plasmas (Ministry of Education) and School of Physics and Astronomy, Collaborative Innovation Center for IFSA (CICIFSA), Shanghai Jiao Tong University, Shanghai 200240, China

<sup>3</sup>Collaborative Innovation Center of Extreme Optics, Shanxi University, Taiyuan, Shanxi 030006, China



(Received 18 October 2018; published 11 June 2019)

The photon-electron angular-momentum transfer is intrinsic and overwhelmingly important in light-molecule interaction. However, the photon-nuclei angular-momentum transfer is seldom observed because of the very large inertial moment and the very small dipole of nuclei as compared to those of the electron. Here, we report the theoretical and experimental observation of the transfer of the spin angular momentum of the photon into the nuclear orbital angular momentum of a molecule. This spin angular-momentum transfer is revealed by carefully examining the emission direction of the ejected proton from the breaking H<sub>2</sub> molecule, which deviates from the initial orientation of the molecular axis. The deviation of the emission direction of the nuclear fragments from the molecular axis depends on its kinetic energy and the ellipticity of the driving laser field, which is confirmed in our numerical simulations.

DOI: [10.1103/PhysRevA.99.063407](https://doi.org/10.1103/PhysRevA.99.063407)

### I. INTRODUCTION

A photon is a massless spin-1 particle, whose helicity and energy govern the most fundamental light-atom and light-molecule interactions. For instance, the polarization is key for producing ultraviolet coherent light [1] and attosecond bursts [2] by switching on or off the electron rescattering; the photon energy is important for triggering photon-induced chemical dynamics of molecules, e.g., reforming and breaking of molecules [3]; and the intrinsic spin angular momentum (SAM) rules the selective photon-induced electron transitions in atoms and molecules.

A photon carrying the SAM of  $\pm\hbar$  is expressed as left- or right-hand circularly polarized light pulses in classical electrodynamics. The SAM of the photons may be transferred to various targets on nano- or atomic scales. For instance, the SAM of the photon can be transferred to its own orbital angular momentum, i.e., a helical vortex wavefront with a phase singularity, via the spin-orbit interaction in artificial topological nanostructures [4] leading to structured optical waves. The SAM transfer (SAMT) can also drive a magnetization dynamics in ferromagnetic nanostructures [5] known as optical spin transfer torque [6]. The SAMT from intense laser fields to atoms is the basis for the generation of SAM-controlled circularly polarized attosecond pulses [7–10]. The angular-momentum transfer in atoms

can be probed by *M*-state-resolved spectroscopy [11,12] via a two-photon process. Recently, pioneering theoretical [13] and experimental [14,15] works observed a field-helicity-dependent photoelectron emission, i.e., spinning photoelectron owing to the strong coupling of the angular momentum of the photons and electrons in strong-field ionization of atoms. As compared to atoms, molecules with additional nuclear freedoms are much more interesting; for instance, the chiral molecule shows a strong circular dichroism [16–18]. However, the coupling of photon helicity and nuclear angular momentum, one of the most fundamental processes in the light-molecule interaction [19–23], is still cryptic.

Here, we demonstrate the SAMT from photons to the nuclear wave packet of a breaking molecule driven by strong laser fields. We create the H<sub>2</sub><sup>+</sup> by singly ionizing a neutral H<sub>2</sub> molecule using a pump pulse, which is afterwards broken by a latterly arrived probe pulse. The distinct momentum distributions of the coincidentally measured electron and ion fragments ejected from a molecule allow us to identify the pump-ionization and probe-dissociation events. The SAM of the photon is coupled to the nuclear wave packet via the route of the photon-electron transfer followed by the electron-nuclei transfer, which is revealed by observing a kinetic-energy-dependent emission direction of the ejected proton from the breaking H<sub>2</sub><sup>+</sup>. Our results demonstrate that not only the electrons but also the nuclei of the molecule will acquire the photon SAM.

The paper is organized as follows. In Secs. II and III, we introduce the experiment methods for the measurement and the numerical models dealing with the dissociative ionization of H<sub>2</sub>. The results are shown in Sec. IV. The paper ends with a conclusion in Sec. V.

\*These authors contributed equally to this work.

† Author to whom correspondence and requests for materials should be addressed: [jwu@phy.ecnu.edu.cn](mailto:jwu@phy.ecnu.edu.cn)

‡ Author to whom correspondence and requests for materials should be addressed: [fhe@sjtu.edu.cn](mailto:fhe@sjtu.edu.cn)

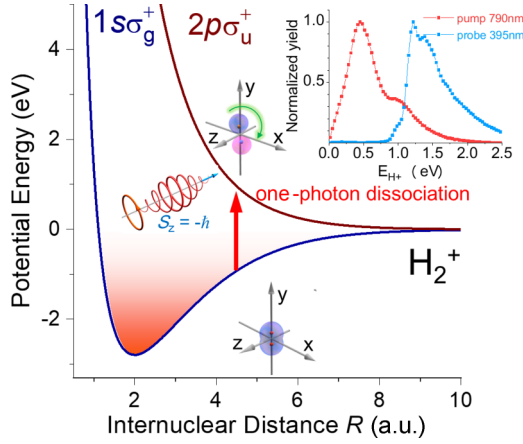


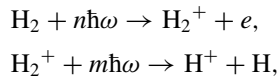
FIG. 1. Schematic diagram of SAMT of left-hand circularly polarized laser pulse with spin angular momentum  $\sigma = -1$  ( $S_z = -\hbar$ ) via the single-photon absorption from the  $1s\sigma_g$  to  $2p\sigma_u$  states in  $H_2^+$ . The inset plot shows the scaled kinetic energy release of  $H^+$  generated in 790 nm (red line) and 395 nm (blue), respectively.

## II. EXPERIMENT METHODS

An elliptically polarized laser field with the ellipticity  $\varepsilon$  and frequency  $\omega$  can be expressed as two counter-rotating circularly polarized laser fields; i.e.,

$$\cos \omega t \vec{e}_x + \varepsilon \sin \omega t \vec{e}_y = \frac{1}{2}(1 + \varepsilon)\vec{\sigma}^+ + \frac{1}{2}(1 - \varepsilon)\vec{\sigma}^-. \quad (1)$$

Here  $\vec{\sigma}^- = \cos \omega t \vec{e}_x - \sin \omega t \vec{e}_y$  and  $\vec{\sigma}^+ = \cos \omega t \vec{e}_x + \sin \omega t \vec{e}_y$  stand for the right- and left-hand circular polarization, and  $S_z = \pm \hbar$  is the spin angular momentum along the laser propagation direction. Exposed to the laser field,  $H_2$  may be singly ionized by absorbing multiple photons, yielding a photoelectron and a molecular cation  $H_2^+$ . As illustrated in Fig. 1, the newborn  $H_2^+$  in the  $1s\sigma_g$  state may absorb extra photons and populate the repulsive  $2p\sigma_u$  state when a time-delayed probe pulse is introduced. These two successive processes are expressed as



where  $n$  and  $m$  are integers. In the first step, the released photoelectron takes almost all photon angular momenta, and the newborn  $H_2^+$  is a spectator in this SAMT. In the second step, the SAM of the probe pulse is deposited into the valence electron of  $H_2^+$  via laser-electron coupling, and afterwards transferred to the ejected protons since the electron attaches on one of the protons.

To examine the SAMT from the photon to the nuclei, we conceive a laser-ellipticity-dependent measurement in the photon-induced dissociation of  $H_2^+$  by completely measuring the three-dimensional momenta of ejected electrons and ions in coincidence, which allows us to unambiguously identify the pump-ionization and probe-dissociation events [24] as illustrated in Fig. 2(a). To prepare the  $H_2^+$  ion source, we use an elliptically polarized ultraviolet femtosecond laser pulse centered at 395-nm to strip one electron from  $H_2$ . A subsequent 790-nm probe pulse is employed to dissociate the  $H_2^+$  that was prepared in the first step. To ensure an

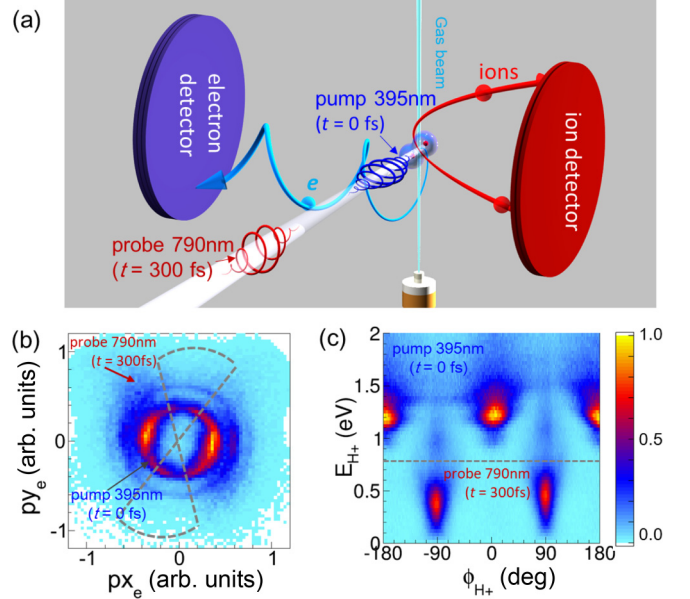


FIG. 2. (a) Sketch of the electron- and proton-momentum measurement from the dissociative ionization of  $H_2$  by a pump pulse (395 nm, blue areas) and a 300-fs time delayed probe pulse (790 nm, red areas). (b) Experimentally measured electron-momentum distribution under the photoionization of pump and probe pulses. The regions enclosed by the gray dashed lines present the independent photoionization from the pump pulse (395 nm). (c) The emission-angle-resolved KER of  $H^+$ . The dissociative fragments induced by the pump pulse and probe pulse are located in the upper and lower half spaces divided by the gray dashed line.

ensemble of randomly orientated  $H_2^+$  for the dissociation by the probe pulse, the pump-probe time delay is set to be 300 fs by avoiding the rotational periods of both  $H_2$  and  $H_2^+$  [25,26].

The experiment was performed in an ultrahigh vacuum reaction microscope of cold target recoil ion momentum spectroscopy (COLTRIMS) [27,28] as illustrated in Fig. 2(a). An ultraviolet 395-nm pump laser pulse was produced by frequency doubling a near-infrared femtosecond laser pulse from a Ti:sapphire multipass amplifier (790 nm, 25 fs, 10 kHz) using a 150- $\mu\text{m}$ -thick  $\beta$ -barium borate ( $\beta$ -BBO) crystal. The collinearly propagating pump and probe pulses were tightly focused onto a supersonic gas jet of  $H_2$  by a concave silver mirror ( $f = 7.5$  cm) inside the COLTRIMS. The peak intensities [29,30] and ellipticity of pump and probe laser pulses in the interaction region were measured to be  $I_{395\text{nm}} \sim 1.0 \times 10^{14} \text{W/cm}^2$ ,  $\varepsilon_{395\text{nm}} = 0.4$  and  $I_{790\text{nm}} \sim 0.85 \times 10^{14} \text{W/cm}^2$ ,  $\varepsilon_{790\text{nm}} = 0.6$ , respectively. The major polarization axes of the pump and probe pulses are along the  $x$  and  $y$  axes, respectively. The rotating sense of the probe pulse can be tuned from left hand to right hand as desired. The photoionization-created ions and electrons were accelerated and guided by a weak homogeneous static electric field and magnetic field. The times of flight of photoelectrons and positions of the impacts were detected by two time- and position-sensitive microchannel plate detectors at the opposite ends of the spectrometer, from which the three-dimensional momenta of the ions and electrons were reconstructed. The electron spectrum is calibrated by examining the discrete photon-energy spaced

photoelectron energy spectrum driven by a single 395-nm laser field in the multiphoton ionization region, and the nuclear spectrum is calibrated using the observed kinetic energy release (KER) value of Coulomb exploded doubly ionized Ar<sub>2</sub>.

As shown in Fig. 2(b), the pump ionization creates a typical photon-energy spaced discrete photoelectron-momentum distribution (PMD) [31] correlated to the H<sub>2</sub><sup>+</sup>, while the elliptically polarized near-infrared (790-nm) ultrashort laser pulse manifests the photoelectron momentum as two moon-like distributions in the *x-y* plane [32]. According to the different PMDs, we are able to spatially select the ionization events from the pump pulse [24] by choosing the regions enclosed by the dashed lines. Besides the distinct PMDs, the ejected H<sup>+</sup> dissociated by the 395-nm pump and 790-nm probe pulses also ends with distinct kinetic energies. As shown in the inset of Fig. 1, the measured H<sup>+</sup> in the energy range of  $E_{H^+} < 0.8$  eV mainly originates from the one-photon dissociation pathway driven by the 790-nm pump pulse, while the high-energy range with  $E_{H^+} > 0.8$  eV is mainly produced by the one-photon dissociation of H<sub>2</sub><sup>+</sup> driven by the 395-nm probe pulse. As shown in Fig. 2(c), by using pump and probe pulses of the orthogonal major polarization axis, the

H<sup>+</sup> from the dissociation by the pump and probe pulses flies to different directions and thus allows us to further spatially disentangle them. Therefore, by properly gating the measured photoelectron and H<sup>+</sup> along different emission directions and kinetic energies, we are able to select the right events induced by the pump ionization and probe dissociation.

### III. NUMERICAL MODELS

Theoretically, we use a hybrid numerical model to simulate the dissociative ionization of H<sub>2</sub>, called strong-field approximation, plus Born-Oppenheimer approximation (SBOA) quantum simulation in the following. The single ionization of H<sub>2</sub> is described by the strong-field approximation, and the dissociation of H<sub>2</sub><sup>+</sup> is modeled by the two-state ( $1s\sigma_g$  and  $2p\sigma_u$ ) time-dependent Schrödinger equation [33]. In this model, the nuclear dynamics is confined in the laser polarization plane. The dissociative ionized molecular wave packet  $\Psi$  after the conclusion of the laser pulse is the product of the freed electron in superimposed Volkov states and the associated H<sub>2</sub><sup>+</sup> in superposed  $1s\sigma_g$  and  $2p\sigma_u$  states. At the terminal time  $t_f$ , the molecular wave packet can be explicitly written as

$$\Psi = \int \frac{d^3k}{(2\pi)^3} |k(t_f)\rangle \otimes \left( |\Psi_{g,k}(t_f)\rangle \right) = -i \int_{t_0}^{t_f} dt' \int \frac{d^3k}{(2\pi)^3} |k(t_f, t')\rangle \otimes U_{\text{dis}}(t_f, t') \left( |\chi_g^0(t_f)\rangle \langle k(t')| \otimes \langle \chi_g^0(t') | H_I(t') | \Phi(t') \rangle \right. \\ \left. + |\chi_u^0(t_f)\rangle \langle kt'| \otimes \langle \chi_u^0(t') | H_I(t') | \Phi(t') \rangle \right), \quad (2)$$

where the Volkov state  $|k(t_f, t')\rangle$  represents the photoelectron born at  $t'$ .  $|\chi_{g/u}^0(t')\rangle$  are the  $1s\sigma_g$ - and  $2p\sigma_u$ -associated nuclear wave packets of H<sub>2</sub><sup>+</sup> at  $t'$ , and are given by the Frank-Condon approximation.  $U_{\text{dis}}(t_f, t')$ , the propagator governing the dissociation of H<sub>2</sub><sup>+</sup>, is written as

$$U_{\text{dis}}(t_f, t') = T \left\{ \exp \left[ -i \int_{t'}^{t_f} dt'' \begin{pmatrix} K_n + V_g & \vec{E} \cdot \vec{D} \\ \vec{E} \cdot \vec{D} & K_n + V_u \end{pmatrix} \right] \right\}, \quad (3)$$

where  $T$  represents the time ordering operator in the coordinate representation,  $K_n = -\frac{1}{2\mu} \frac{\partial^2}{\partial R^2}$  is the operator of the nuclear kinetic energy,  $\mu$  is the reduced mass for two protons,  $V_g$  and  $V_u$  are the energy curves of the  $1s\sigma_g$  and  $2p\sigma_u$  states, and  $\vec{D}$  is the dipole coupling matrix between  $1s\sigma_g$  and  $2p\sigma_u$  states. The dissociated nuclear-momentum distribution is obtained by integrating  $\int d^3k [|\Psi_{g,k}(p_R)|^2 + |\Psi_{u,k}(p_R)|^2]$ , where  $\Psi_{g/u,k}(p_R) = \langle p_R | \Psi_{g/u,k} \rangle$  and  $p_R$  is the nuclear momentum. Note that the correlation of the ionization of H<sub>2</sub> and the dissociation of H<sub>2</sub><sup>+</sup> is preserved in this model.

With the dissociative molecular wave packet  $\Psi$  in hand, the angular momentum of the ejected nuclear fragments along the laser propagation is calculated via  $\langle \vec{M} \rangle_z = \langle \Psi | L_z | \Psi \rangle$  where  $L_z$  is the nuclear orbital angular-momentum operator. The pump and probe pulses are expressed as

$$E_{\text{pump}}(t) = E_{\text{pump}}(t) (\cos \omega t \vec{e}_x + \varepsilon_{\text{pump}} \sin \omega t \vec{e}_y), \quad (4)$$

$$\vec{E}_{\text{probe}}(t) = E_{\text{probe}}(t) (\varepsilon_{\text{probe}} \cos \omega t \vec{e}_x \pm \sin \omega t \vec{e}_y), \quad (5)$$

with the major axis along the *x* and *y* directions, respectively, where  $\varepsilon_{\text{pump}}$  and  $\varepsilon_{\text{probe}}$  denote the ellipticity of the pump and probe pulses. The laser fields used in simulations are same as those used in the experiment.

### IV. RESULTS AND DISCUSSIONS

Since the right- and left-hand polarized probe pulse should deposit opposite angular momenta into the molecule, one may expect that the probe pulses with different helicity will induce different proton-momentum distributions. Figure 3(a) shows the calculated proton-momentum distribution for the laser ellipticity of  $\varepsilon_{\text{probe}} = 0.6$ . The emission direction of the proton slightly deviates from the major axis (along the *y* axis) of the driving laser pulse. To highlight the deviation, we defined a differentially normalized asymmetric momentum distribution,

$$\beta(p_x, p_y) = \frac{W_{\text{LH}}(p_x, p_y) - W_{\text{RH}}(p_x, p_y)}{W_{\text{LH}}(p_x, p_y) + W_{\text{RH}}(p_x, p_y)}. \quad (6)$$

Here  $W_{\text{LH}}(p_x, p_y)$  and  $W_{\text{RH}}(p_x, p_y)$  are the yields of the one-photon dissociation of H<sub>2</sub><sup>+</sup> induced by the left- and right-hand elliptically polarized laser fields, respectively. We use  $\delta\theta_{H^+}$  to denote the deviation angle of the emitted nuclear fragments from the major axis of the elliptically polarized laser field. Figure 3(b) presents the simulated  $\beta(p_x, p_y)$  for  $\varepsilon_{\text{probe}} = 0.6$  where a clear left-right asymmetry is observed. As shown in Fig. 3(c), after absorbing one photon and jumping from the  $1s\sigma_g$  state to the  $2p\sigma_u$  state, the dissociated nuclear wave packet acquires the angular momentum from the driving laser

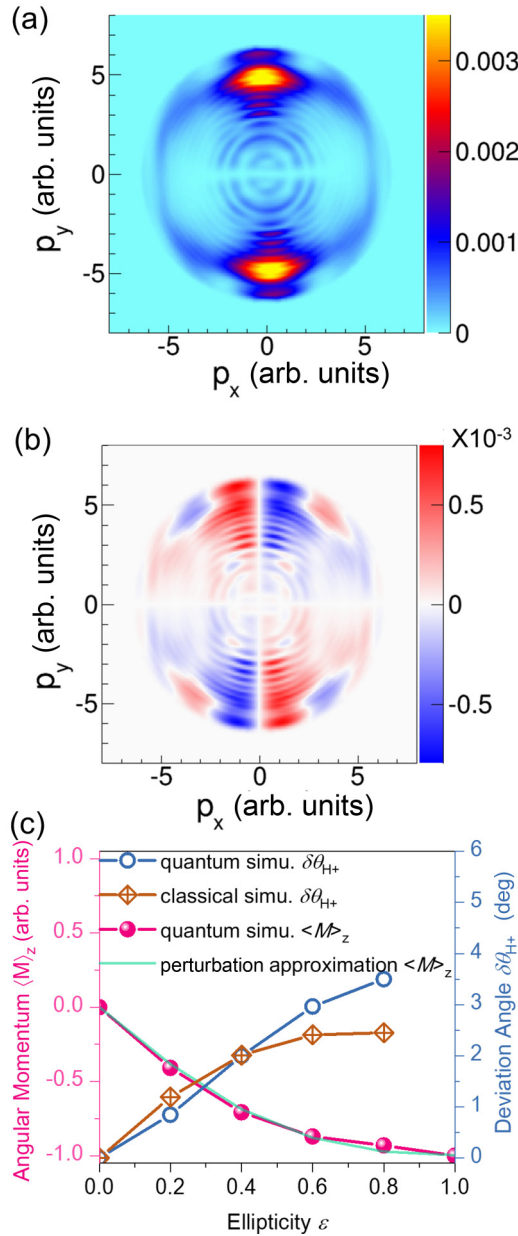


FIG. 3. (a) Numerically simulated momentum distribution of emitted protons driven by a left-hand elliptically polarized laser field with ellipticity of 0.6. (b) Differentially normalized momentum distribution  $\beta(p_x, p_y)$  of protons driven by left- and right-hand elliptically polarized laser fields with ellipticity of  $\pm 0.6$ . (c) Calculated angular momentum  $\langle \vec{M} \rangle_z$  and deviation angle  $\delta\theta_{H^+}$  of  $H^+$  as a function of laser ellipticity.

field and  $\delta\theta_{H^+}$  increases gradually with the increasing of the ellipticity of the probe pulse.

For the one-photon transition, as shown in Eq. (3), the laser- $H_2^+$  coupling Hamiltonian is proportional to  $(1 + \epsilon)\vec{\sigma}^- \cdot \vec{D} + (1 - \epsilon)\vec{\sigma}^+ \cdot \vec{D}$ , and the Wigner-Eckart theorem implies that the one-photon dissociation wave function could be perturbatively represented by  $|\Psi\rangle \propto (1 + \epsilon)|m = +1\rangle + (1 - \epsilon)|m = -1\rangle$ , where  $m$  is the magnetic quantum number. Therefore, the expected angular momentum along the laser propagation is given by  $m_z =$

$\frac{\langle \Psi | M_z | \Psi \rangle}{\langle \Psi | \Psi \rangle} = \frac{2\epsilon}{1 + \epsilon^2}$  with  $M_z$  being the longitudinal component of the angular-momentum operator. Such a perturbative calculation is comparable with the SBOA quantum simulation, as shown in Fig. 3(c). This intrinsic angular momentum is encoded into the deviation angle  $\delta\theta_{H^+}$ . Though protons with different energies have different  $\delta\theta_{H^+}$  due to the motion of nuclei, comparing  $\delta\theta_{H^+}$  at a fixed energy with ellipticity  $\epsilon_{\text{probe}} = 0.6$  and  $\epsilon_{\text{probe}} = 0.4$  makes it possible to infer the intrinsic spin angular momentum.

Furthermore, the deviation angle  $\delta\theta_{H^+}$  can be estimated by constructing a model of the classical rotor. Assuming that  $H_2^+$  starts to dissociate at  $R_0$  where the one-photon resonant coupling between  $1s\sigma_g$  and  $2p\sigma_u$  occurs, one may deduce

$$\delta\theta_{H^+} = \int_{R_0}^{\infty} \frac{M}{I} \frac{dR}{dt} dR, \quad (7)$$

where  $I = 2\mu R^2$  and  $M = I \frac{d\theta}{dt}$  are the rotational inertia and angular momentum of the molecular ion. Here  $\frac{dR}{dt}$  is the repulsive velocity, which can be obtained by assuming a classical particle propagates on the  $2p\sigma_u$  potential curve from  $R_0$  by numerically solving the Newtonian equation. Such a classical estimation gives the similar  $\delta\theta_{H^+}$  as shown in Fig. 3(c) (cyan diamonds). The calculated  $\delta\theta_{H^+}$  is independent of the laser intensity and the molecular orientation, which contradicts the well-accepted scenario of the electric kick and supports the SAMT.

Figure 4(a) displays the experimentally measured proton-momentum distribution induced by one-photon dissociation of  $H_2^+$  in the  $y$ - $z$  plane driven by the probe pulse with ellipticity of  $\epsilon_{\text{probe}} = 0.6$ . The corresponding differentially normalized distribution is shown in Fig. 4(c). Figures 4(b) and 4(d) display the measured proton-momentum distribution and its differential normalization when the ellipticity of the probe pulse varies from 0.6 to 0.4. A smaller ellipticity leads to a smaller  $\delta\theta_{H^+}$ . As shown in Fig. 5(a), the emission angle of the ejected nuclear fragments increases with the decreasing of the proton energy. Here the one-photon dissociation of  $H_2^+$  can be understood as the absorption of a left-hand photon and a right-hand photon of various strength ratios depending on the ellipticity of the probe pulse. A maximum emission angle of  $\phi_{H^+} = 94 \pm 1^\circ (92 \pm 2^\circ)$  is observed at  $E_{H^+} = 0.15$  eV, corresponding to  $\delta\theta_{H^+} = 4 \pm 1^\circ (2 \pm 2^\circ)$  with respect to the major axis of probe pulse for  $\epsilon_{\text{probe}} = 0.6(0.4)$ . The error bar is calculated by using Gauss's error propagation law based on the uncertainty of the normalized differences, i.e.,

$$\Delta(\overline{LH}, \overline{RH}) = 2 \sqrt{\frac{\overline{LH} \times \overline{RH}}{(\overline{LH} + \overline{RH})^3}},$$

where  $\overline{LH}$  and  $\overline{RH}$  contain absolute numbers of counts. Our numerical simulation mainly reveals the KER-dependent deviation in high-KER regions. As shown in Fig. 3(c), the average deviation angle of  $3^\circ (2^\circ)$  for  $\epsilon_{\text{probe}} = 0.6(0.4)$  indicates an average nuclei angular-momentum variation  $\langle \vec{M} \rangle_z = 0.87(0.70)$  through the SAMT. The deviation angle  $\delta\theta_{H^+}$  gradually decreases to  $1^\circ$  with increasing  $E_{H^+}$  up to 0.6 eV, as shown in Figs. 5(a) and 5(b). The deviation between simulation and experiment in the KER region of  $E_{H^+} < 0.3$  eV might originate from the Frank-Condon approximation for the description of the nuclear wave packet. The numerically simulated kinetic energy in the

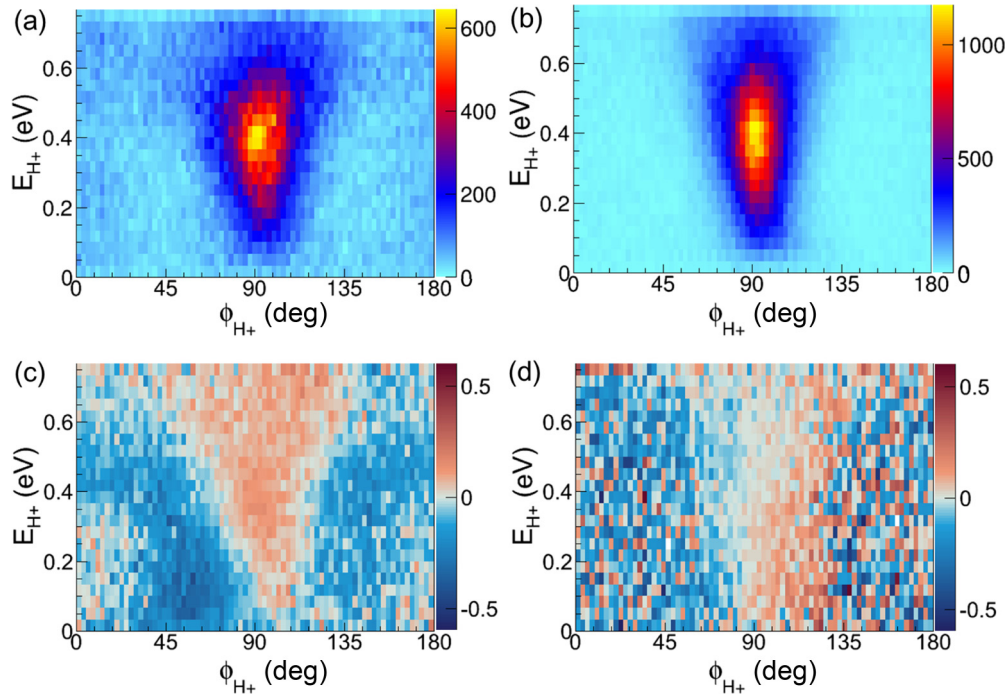


FIG. 4. (a,b) Experimentally measured proton emission direction  $\phi_{H^+}$  as a function of  $E_{H^+}$  in the  $x$ - $y$  plane under the clockwise elliptically polarized probe laser field with ellipticity of (a)  $\varepsilon_{\text{probe}} = 0.6$  and (b)  $\varepsilon_{\text{probe}} = 0.4$ , respectively. (c,d) The same as in (a,b) but for differential normalization  $\beta(p_x, p_y)$ .

low-energy regime is smaller than that observed in the experiment. Besides that, the Coulomb action on the photoelectron is also neglected in the simulation, which further modifies the coherence of  $H_2^+$  produced at a different time. Compared to the classical or the quantum calculations without considering the single ionization of  $H_2$ , this SBOA model can reproduce the experimental measurement qualitatively. The acceptable agreement supports the SAMT principle: The photon SAM is transferred to the bound electron during the photon-coupled transition from the  $1s\sigma_g$  state to the  $2p\sigma_u$  state of  $H_2^+$ , and afterwards the electron angular-momentum deposits onto the heavy nuclei during the stretching of the molecular bond via the electron-nuclei Coulomb interaction. The more energetic protons have smaller  $\delta\theta_{H^+}$ , which can be understood intuitively based on Eq. (7). The dissociation

initiated at the shorter internuclear distance will experience a faster motion of nuclei ( $dR/dt$ ) and quickly increasing rotary inertia  $I$ , and thus lead to a smaller deviation angle.

## V. CONCLUSION

We experimentally and theoretically demonstrated the SAMT from photon to nuclei in the prototype system of one-photon-coupled dissociation of  $H_2^+$ . Driven by an elliptically polarized laser pulse, the spinning of the nuclear wave packet [34] during dissociation must be taken into account in order to precisely analyze ultrafast processes, such as the attoclock [32] molecular tunneling ionization, and circular dichroisms in angular distribution [17] or in molecular frame [19,35]. The SAMT can provide an extra dimension

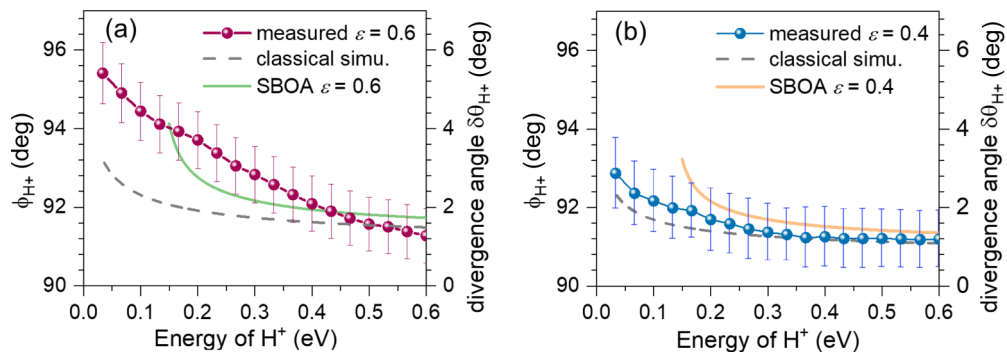


FIG. 5. Experimentally measured and theoretically simulated proton emission angle as a function of the kinetic energy of the proton ( $E_{H^+}$ ) for different ellipticities of (a)  $\varepsilon_{\text{probe}} = 0.6$  and (b)  $\varepsilon_{\text{probe}} = 0.4$ , where  $\phi_{H^+}$  and  $d\theta_{H^+}$  indicate the directly measured emission angle in the  $x$ - $y$  plane and the deviation angle from the major axis of the dissociation laser field, respectively. The gray dashed lines and green and orange solid lines are extracted from classical rotor model and SBOA quantum simulation, respectively.

to probe and control the spin-related photoemission dynamics and may open a new route to understanding electron-nuclear correlation and rearrangement of molecules in strong laser fields.

#### ACKNOWLEDGMENTS

This work is supported by the National Key R&D Program of China (Grants No. 2018YFA0306303 and

No. 2018YFA0404802), the National Natural Science Foundation of China (Grants No. 11425416, No. 61690224, No. 11621404, No. 11574205, No. 11721091, No. 91850203, No. 11834004, and No. 11804098), Innovation Program of Shanghai Municipal Education Commission (Grant No. 2017-01-07-00-02-E00034), and Shanghai Shuguang Project (Project No. 17SG10). Simulations were performed on the  $\pi$  supercomputer at Shanghai Jiao Tong University.

- 
- [1] P. Dietrich, N. H. Burnett, M. Ivanov, and P. B. Corkum, High-harmonic generation and correlated two-electron multiphoton ionization with elliptically polarized light, *Phys. Rev. A* **50**, R3585 (1994).
- [2] M. Hentschel, R. Kienberger, Ch. Spielmann, G. A. Reider, N. Milosevic, T. Brabec, P. Corkum, U. Heinzmann, M. Drescher, and F. Krausz, Attosecond metrology, *Nature* **414**, 509 (2001).
- [3] M. F. Kling *et al.*, Control of electron localization in molecular dissociation, *Science* **312**, 246 (2006).
- [4] L. Marrucci, C. Manzo, and D. Paparo, Optical Spin-to-Orbital Angular Momentum Conversion in Inhomogeneous Anisotropic Media, *Phys. Rev. Lett.* **96**, 163905 (2006).
- [5] N. Bergeard, V. López-Flores, V. Halté, M. Hehn, C. Stamm, N. Pontius, E. Beaurepaire, and C. Boeglin, Ultrafast angular momentum transfer in multisublattice ferrimagnets, *Nat. Commun.* **5**, 3466 (2014).
- [6] P. Němec *et al.*, Experimental observation of the optical spin transfer torque, *Nat. Phys.* **8**, 411 (2012).
- [7] D. D. Hickstein *et al.*, Non-collinear generation of angularly isolated circularly polarized high harmonics, *Nat. Photonics* **9**, 743 (2015).
- [8] O. Kfir *et al.*, Generation of bright phase-matched circularly-polarized extreme ultraviolet high harmonics, *Nat. Photonics* **9**, 99 (2015).
- [9] D. B. Milošević, W. Becker, and R. Kopold, Generation of circularly polarized high-order harmonics by two-color coplanar field mixing, *Phys. Rev. A* **61**, 063403 (2000).
- [10] E. Prost, H. Zhang, E. Hertz, F. Billard, B. Lavorel, P. Bejot, J. Zyss, I. S. Averbukh, and O. Faucher, Third-order-harmonic generation in coherently spinning molecules, *Phys. Rev. A* **96**, 043418 (2017).
- [11] N. Dudovich, D. Oron, and Y. Silberberg, Quantum Control of the Angular Momentum Distribution in Multiphoton Absorption Processes, *Phys. Rev. Lett.* **92**, 103003 (2004).
- [12] D. A. Malik, A. V. Kimel, A. Kirilyuk, T. Rasing, and W. J. van der Zande, Coherent Control of Angular Momentum Transfer in Resonant Two-Photon Light-Matter Interaction, *Phys. Rev. Lett.* **104**, 133001 (2010).
- [13] I. Barth and O. Smirnova, Nonadiabatic tunneling in circularly polarized laser fields: Physical picture and calculations, *Phys. Rev. A* **84**, 063415 (2011).
- [14] T. Herath, L. Yan, S. K. Lee, and W. Li, Strong-Field Ionization Rate Depends on the Sign of the Magnetic Quantum Number, *Phys. Rev. Lett.* **109**, 043004 (2012).
- [15] A. Hartung *et al.*, Electron spin polarization in strong-field ionization of xenon atoms, *Nat. Photonics* **10**, 526 (2016).
- [16] B. Ritchie, Theory of the angular distribution of photoelectrons ejected from optically active molecules and molecular negative ions, *Phys. Rev. A* **13**, 1411 (1976).
- [17] I. Powis, Photoelectron spectroscopy and circular dichroism in chiral biomolecules: l-alanine, *J. Phys. Chem. A* **104**, 878 (2000).
- [18] A. Ferré *et al.*, A table-top ultrashort light source in the extreme ultraviolet for circular dichroism experiments, *Nat. Photonics* **9**, 93 (2014).
- [19] D. Dówek, J. F. Pérez-Torres, Y. J. Picard, P. Billaud, C. Elkharrat, J. C. Houver, J. L. Sanz-Vicario, and F. Martín, Circular Dichroism in Photoionization of H<sub>2</sub>, *Phys. Rev. Lett.* **104**, 233003 (2010).
- [20] P. L. Houston, Vector correlations in photodissociation dynamics, *J. Phys. Chem.* **91**, 5388 (1987).
- [21] J. P. Simons, Dynamical stereochemistry and the polarization of reaction products, *J. Phys. Chem.* **91**, 5378 (1987).
- [22] L. D. A. Siebbeles, M. Glass-Maujean, O. S. Vasyutinskii, J. A. Beswick, and O. Roncero, Vector properties in photodissociation: Quantum treatment of the correlation between the spatial anisotropy and the angular momentum polarization of the fragments, *J. Chem. Phys.* **100**, 3610 (1994).
- [23] T. P. Rakitzis, S. A. Kandel, and R. N. Zare, Determination of differential-cross-section moments from polarization-dependent product velocity distributions of photoinitiated bimolecular reactions, *J. Chem. Phys.* **107**, 9382 (1997).
- [24] Q. Song, Z. Li, S. Cui, P. Lu, X. Gong, Q. Ji, K. Lin, W. Zhang, J. Ma, H. Pan *et al.*, Disentangling the role of laser coupling in directional breaking of molecules, *Phys. Rev. A* **94**, 053419 (2016).
- [25] I. A. Bocharova, H. Mashiko, M. Magrakvelidze, D. Ray, P. Ranitovic, C. L. Cocke, and I. V. Litvinyuk, Direct Coulomb-explosion imaging of coherent nuclear dynamics induced by few-cycle laser pulses in light and heavy hydrogen, *Phys. Rev. A* **77**, 053407 (2008).
- [26] F. Anis, T. Cackowski, and B. D. Esry, Rotational dynamics of dissociating H<sub>2</sub><sup>+</sup> in a short intense laser pulse, *J. Phys. B* **42**, 091001 (2009).
- [27] R. Dörner, V. Mergel, O. Jagutzki, L. Spielberger, J. Ullrich, R. Moshhammer, and H. Schmidt-Böcking, Cold Target Recoil Ion Momentum Spectroscopy: A ‘momentum microscope’ to view atomic collision dynamics, *Phys. Rep.* **330**, 95 (2000).
- [28] J. Ullrich, R. Moshhammer, A. Dorn, R. Dörner, L. Ph. H. Schmidt, and H. Schmidt-Böcking, Recoil-ion and electron momentum spectroscopy: Reaction-microscopes, *Rep. Prog. Phys.* **66**, 1463 (2003).
- [29] A. S. Alnaser, X. M. Tong, T. Osipov, S. Voss, C. M. Maharjan, B. Shan, Z. Chang, and C. L. Cocke, Laser-peak-intensity calibration using recoil-ion momentum imaging, *Phys. Rev. A* **70**, 023413 (2004).
- [30] K. Henrichs, M. Waitz, F. Trinter, H. Kim, A. Menssen, H. Gassert, H. Sann, T. Jahnke, J. Wu, M. Pitzer, M. Richter,

- M. S. Schöffler, M. Kunitski, and R. Dörner, Observation of Electron Energy Discretization in Strong Field Double Ionization, *Phys. Rev. Lett.* **111**, 113003 (2013).
- [31] X. Gong *et al.*, Pathway-resolved photoelectron emission in dissociative ionization of molecules, *Optica* **3**, 643 (2016).
- [32] P. Eckle, A. N. Pfeiffer, C. Cirelli, A. Staudte, R. Dörner, H. G. Muller, M. Büttiker, and U. Keller, Attosecond ionization and tunneling delay time measurements in helium, *Science* **322**, 1525 (2008).
- [33] F. He and U. Thumm, Dissociative ionization of H<sub>2</sub> in an attosecond pulse train and delayed laser pulse, *Phys. Rev. A* **81**, 053413 (2010).
- [34] J. Karczarek, J. Wright, P. Corkum, and M. Ivanov, Optical Centrifuge for Molecules, *Phys. Rev. Lett.* **82**, 3420 (1999).
- [35] M. Tia *et al.*, Observation of enhanced chiral asymmetries in the inner-shell photoionization of uniaxially oriented methyloxirane enantiomers, *J. Phys. Chem. Lett.* **8**, 2780 (2017).